PCCP

PAPER

View Article Online
View Journal | View Issue

Cite this: *Phys. Chem. Chem. Phys.*, 2024, **26**, 26022

Tailoring van der Waals interactions in ultra-thin two dimensional metal–organic frameworks (MOFs) for photoconductive applications†

David Dell'Angelo, *[a] Ioannis Karamanis,[a] Mohammad Reza Saeb,[b] Lavinia Balan *[c] and Michael Badawi *[a]

Received 27th August 2024,
Accepted 26th September 2024

DOI: 10.1039/d4cp03347g

rsc.li/pccp

The diverse structural tunability of 2-dimensional π-stacked layered metal–organic frameworks (2D MOFs) enables the control of charge carrier mobility to achieve specific photoconductive characteristics. This study demonstrates the potential of various theoretical methodologies and frameworks in establishing a correlation between structure and functionality for such purposes. Through a focus on the archetypal $Ni_3(HITP)_2$ 2D MOF, we examine the impact of quantum confinement and stacking fault defects on the absorption spectra using our recently-developed Frenkel–Holstein Hamiltonian. Specifically, the relationship between optical properties and number of layer units along the π-stacking direction is discussed. We employ Marcus rate theory to evaluate vertical carrier mobility subject to inter-layer proximity and different crystal packing which affect van der Waals interactions between layers. The insights presented in this research can inform the development of guidelines for enhancing photoconductive properties in 2D MOF nanosheets.

1. Introduction

Besides their distinctive conductive properties,[1,2] two-dimensional (2D) metal–organic frameworks (MOFs) have garnered increased research interest recently due to their potential application as photocatalytic materials exhibiting tunable electronic and optical characteristics.[3–5] As shown in Fig. 1(a), in 2D MOFs atoms are arranged into layers held together by in-plane covalent or coordinative bonds. These layers are subsequently arranged in the out-of-plane direction with relatively weak van der Waals (vdW) interactions, resulting in the formation of parallel 1D channels. This specific architecture facilitates bulk exfoliation and nanosheet manufacturing, even down to a single layer.[6,7] Consequently, in comparison to their 3D bulk counterparts, 2D MOFs present ultra-thin thickness,[6] large surface area[8] and effective charge separation,[9] all of which facilitate the efficient transfer of captured energy to external acceptors, thereby enhancing the photocatalytic performance of the material.[10] Indeed, 2D MOFs may exhibit non-zero band

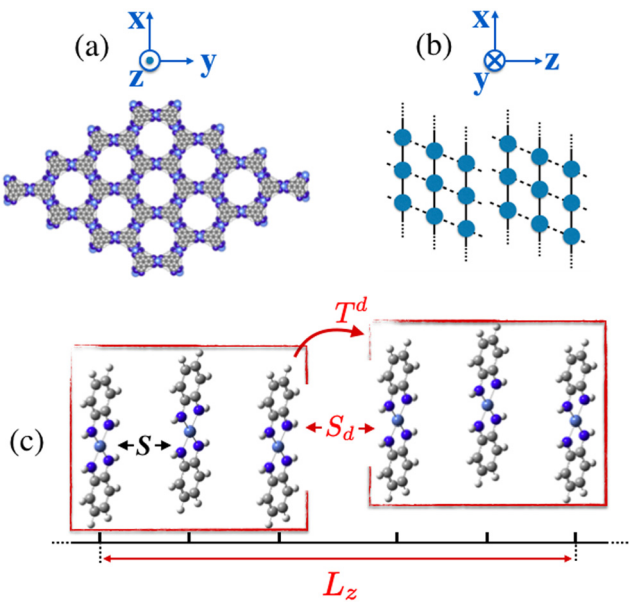

Fig. 1 (a) Crystal structure of the 2D layered $Ni_3(HITP)_2$ (HITP = 2, 3, 6, 7, 10, 11-hexaiminotriphenylene) MOF with hexagonal 1D channels along the π-stacking direction. (b) Schematic diagram of the layer–layer displacement defect (stacking fault) along the π-stacking as in reference Foster *et al.*[13] (c) A representative reduced model of $Ni_3(HITP)_2$ employed in this work with parameters S and S_d monitoring inter-layer and stacking fault spacings between units, respectively. Finally, L_z controls the vertical π-stacking length.

[a] *Université de Lorraine, CNRS, L2CM, F-57000 Metz, France. E-mail: david.dell-angelo@univ-lorraine.fr, Michael.badawi@univ-lorraine.fr*
[b] *Department of Pharmaceutical Chemistry, Medical University of Gdańsk, J. Hallera 107, 80-416 Gdańsk, Poland*
[c] *CEMHTI-UPR 3079 CNRS, Site Haute Température, 1D avenue de la Recherche Scientifique, 45071 Orl éans, France. E-mail: lavinia.balan@cnrs-orleans.fr*

† Electronic supplementary information (ESI) available. See DOI: https://doi.org/10.1039/d4cp03347g

gaps,[11] *i.e.*, semiconductive behaviour, as shown by their intrinsic temperature dependent electrical conductivity.[11,12]

This semiconductive characteristic was recently corroborated by our computational analysis of electronic properties[14] for the archetypal layered MOF $Ni_3(HITP)_2$ (HITP = 2, 3, 6, 7, 10, 11-hexaiminotriphenylene).[11,15,16] Through *ab initio* molecular dynamics (AIMD) simulations and subsequent band structure calculations, we have shown that finite temperature induces a competition between the openings of direct and indirect band gaps in 2D layered MOFs.[14]

Hence, generation and recombination rates of photo-induced electron–hole (e–h) pairs in 2D MOFs depend on both the wavelength-dependent absorption rate and the energy conservation balance at the Fermi level. Nevertheless, understanding structure–property relationships in 2D layered MOFs is essentially in its early stages. Atomistic-level insights created by theoretical studies can provide guidelines to significantly improve the photoconductive properties of these intriguing systems. Indeed, AIMD methods can provide complementary insights while also explicitly accounting for the finite temperature.[17] One of the questions to be addressed, before any compact device implementation, is how the spatial confinement affects charge transport and optical properties in ultra-thin 2D MOFs.[18,19] Another critical inquiry involves the correlation between charge transport and crystal packing along the stacking direction as well as whether the vdW interactions can be enhanced by tuning the crystal packing of the layered architecture. In this context, we have very recently shown[20] that the inter-layer overlap of the electronic wavefunctions and thus the transfer integral (t) in 2D MOFs is intricately dependent on both the inter-layer distance and orientation of the layers and scales with the reorganization energy (λ). Herein, using the archetypal $Ni_3(HITP)_2$ 2D MOF, we elaborate on how spatial confinement and inter-layer proximity[21] along the π-stacking may be tailored in order to modulate optical properties and vertical mobility in ultra-thin 2D MOFs. The theoretical model is summarized in the next section. Section 3 introduces the stacking fault Hamiltonian. Section 4 provides the results and the associated discussions on absorption spectra and mobility.

2. The model

To study the effect of confinement and stacking fault defects[13] on optical properties and carrier mobility of 2D MOFs, we design a model of $Ni_3(HITP)_2$ system as demonstrated in Fig. 1(c). This model consists of a linear array of $N + 1$ secondary building units (SBUs)[20,22] along the non-covalent π-stacking direction. The length of this stack of SBUs is defined as L_z while S and S_d parameters corresponds to the inter-layer spacing between the two SBU units and to the stacking fault spacing, respectively. Due to the optical invariance with respect to the relative in plane sliding, the triphenylene organic linkers in each unit were truncated to benzene rings.[20] Given the ability in molybdenum disulfide to tune the band gap as a function of the number of layers and to detect the light at different wavelengths,[23] we first investigate how the optical response may vary with the thickness L_z. For this purpose, we use the Holstein Hamiltonian[24–26] that has been recently employed to study the absorption spectrum of $Ni_3(HITP)_2$.[20] We have shown that this Hamiltonian, containing the phonon coupling at finite temperature, can provide an accurate description of the carrier hopping between building units of 2D frameworks.

3. The Hamiltonian

The Hamiltonian is comprised of four terms:

$$H = H_J + H_T + H_{POL} + H_D \tag{1}$$

where the first term includes the vibronic coupling (the Frenkel term), the second term accounts for electron and hole transfers and the third term includes the energies of the polaronic states and their associated vibronic couplings (more details can be found in reference dell'Angelo *et al.*[20]). The last term takes into account the stacking fault defect as represented in Fig. 1(c):

$$H_D = H_T^d + H_{POL}^d \tag{2}$$

The first term of eqn (2) accounts for electron and hole transfers at the stacking fault:

$$\begin{aligned} H_T^d &= t_e^d\big(|c_N, a_{N+S_d}\rangle\langle c_N, a_{N+S_d+1}| \\ &\quad + |c_N, a_{N+S_d}\rangle\langle c_N, a_{N+S_d-1}|\big) \\ &\quad + t_h^d\big(|c_N, a_{N+S_d}\rangle\langle c_{N+1}, a_{N+S_d}| \\ &\quad + |c_N, a_{N+S_d}\rangle\langle c_{N-1}, a_{N+S_d}|\big) \end{aligned} \tag{3}$$

where t_e^d and t_h^d represent the transfer integrals which arise from HOMO–HOMO and LUMO–LUMO interactions between nearest neighbour SBUs and decay exponentially with distance S_d. The second term in eqn (2) includes the energies of the polaronic states and their associated vibronic couplings:

$$\begin{aligned} H_{POL}^d &= E_T^d|c_N, a_{N+S_d}\rangle\langle c_N, a_{N+S_d}| + \hbar\omega_0\lambda_+^d \\ &\quad \times \left(b_N^\dagger + b_N + \lambda_+^d\right)|c_N, a_{N+S_d}\rangle\langle c_N, a_{N+S_d}| + \hbar\omega_0\lambda_-^d \\ &\quad \times \left(b_{N+S_d}^\dagger + b_{N+S_d} + \lambda_-^d\right)|c_N, a_{N+S_d}\rangle\langle c_N, a_{N+S_d}| \end{aligned} \tag{4}$$

where the E_T^d energy is a function of the separation (S_d) between the hole on monomer N and the electron on monomer $N + S_d$, whereas the second and the third term of eqn (4) monitor the local vibrational coupling quantified by the dimensionless $\lambda_{(+/-)}^d$ factors. The effective coupling between units is provided by the interference of the charge transfer T with the exciton Coulomb coupling J_{Coul} and can be either constructive or destructive, according to the expression:[27]

$$J_{eff} = J_{Coul} + T^{(d)} \tag{5}$$

where

$$T^{(d)} = -2\frac{t_e \times t_h}{E_{TS_1}}. \tag{6}$$

$E_{T\text{-}S_1}$ in eqn (6) is the difference between the charge transfer energy and the energy of the $S_0 \rightarrow S_1$ electronic transition. t_e and t_h stand for electron and hole transfer integrals and monitor the strength of the interaction and the ease of charge transfer within a dimer made of two consecutive units (the apex *d* referring to the interaction at the stacking fault). They are obtained by calculating the dimer Hamiltonian in the atomic orbital basis from the Roothaan equation:

$$\mathbf{H}_{AO} = \mathbf{SCEC}^{-1} \quad (7)$$

where **S** is the overlap matrix and the matrix C corresponds to the supramolecular orbitals of the dimer. Eqn (6) implies a two-step super exchange process[28] in which the exciton moves between two consecutive units *via* a virtual charge transfer state. Since in our model we assume $E_{T\text{-}S_1} > 0$, T can be positive or negative depending on the sign of the product $t_p = t_e \times t_h$. Hence, the relative sign between t_e and t_h controls the J- and H-like photophysical properties in layered MOF aggregates. Here, J stands for induced red shift[29] whereas H stands for induced blue shift[30] as a result of the aggregation.

4. Results and discussion

In order to elucidate the correlation between spatial confinement and properties in thin 2D-MOF, this section is divided into two segments: the initial one underscores the optical characteristics, while the subsequent one delves into the vertical mobility within the stacking model.

4.1. Modulation of the absorbance spectrum

4.1.1. Effect of the quantum confinement on the spectra. Fig. 2 shows the absorption spectrum of a bulk model of $Ni_3(HITP)_2$ comprised of a 1D stack of $N = 30$ SBU monomers in navy blue against the experimental spectrum in black where the Holstein Hamiltonian reproduces the position and intensity of peaks in the experimental spectrum. The Hamiltonian also provides us with means to study the effect of quantum confinement along L_z by monitoring the ratio between the first two vibronic peaks of the spectra A_1 and A_2 relative to 0–0/0–1 ratio of the monomer.[20] It has been already reported[25,31] that the ratio of the first two peaks of the absorption spectrum (A_1/A_2) depends on the nature of the coulombic coupling. In particular, this ratio increases with the magnitude of the intermolecular coupling in J-aggregates ($J_{Coul} < 0$, red shift) and decreases in H-aggregates ($J_{Coul} > 0$, blue shift). After careful inspection of the convergence with respect to the number of vibrational quanta for Frenkel and charge transfer states (see Fig. 3), the onset in Fig. 2 shows that by decreasing L_z to 6 and 3 nm the A_1/A_2 ratio decreases which is an H-aggregate feature. This indicates how photophysical properties of 2D MOFs may be tailored by progressive exfoliation.

4.1.2. Tailoring the absorption peaks. Additionally, the A_1/A_2 ratio may be further refined *via* engineering the energy difference $E_{T\text{-}S_1}$. Fig. 4 shows how the optical response of the model $Ni_3(HITP)_2$ evolves in two different regimes: *R*, the resonance regime where $E_T \approx E_{S_1}$, and qR, the quasi-resonance regime where $E_T \approx 1.5E_{S_1}$. All parameters used in these simulations are reported in Table S1 in the ESI.† The left panel of Fig. 4 displays a notable linear increase in the A_1/A_2 ratio as a function of the charge transfer product t_p, inducing a J-like feature[31] in both regimes. Although the resonance regime shows an overall higher A_1/A_2 ratio than the quasi-resonance regime, these ratios are closer at small transfer integral values, in particular when $t_p \sim 2.5 \times 10^5$ cm^{-1}. At $t_p > 5 \times 10^5$ cm^{-1} an increasing divergence of the ratios calculated at two regimes is observed,

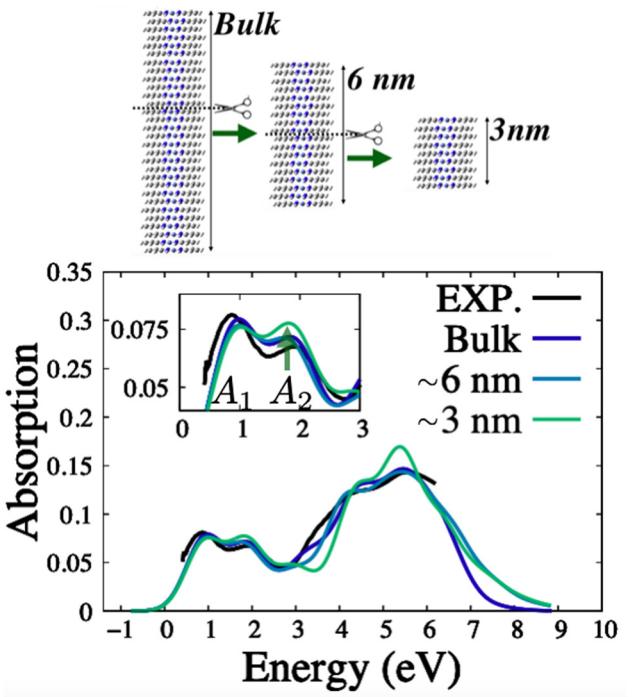

Fig. 2 Calculated absorption spectra as a result of exfoliating $Ni_3(HITP)_2$ along the vertical dimension L_z. Provided the experimental[15] inter-layer spacing $S = 3.3$ Å (see Fig. 1b), the illustrated quantum confinement models correspond to $L_z = 5.94$ nm and $L_z = 2.97$ nm and are comprised of 18 and 9 units, respectively. The experimental profile is taken from reference Sheberla *et al.*[11] The remainder of the parameters are $J_{Coul} = 1100$, $t_h = 910$, $t_e = 875$ and $E_{T\text{-}S_1} = 1400$ cm^{-1}.

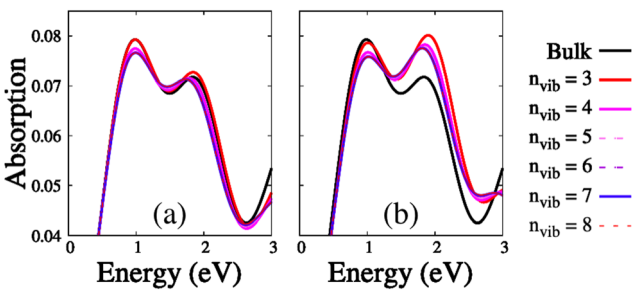

Fig. 3 Provided the onset of the spectra in Fig. 2, these profiles show the convergence with respect to the number of vibrational quanta for Frenkel and charge transfer states as a result of exfoliating $Ni_3(HITP)_2$ along the vertical dimension (a) $L_z = 5.94$ nm and (b) $L_z = 2.97$ nm. The converged profiles ($n_{vib} = 7$) were then used for generating Fig. 2.

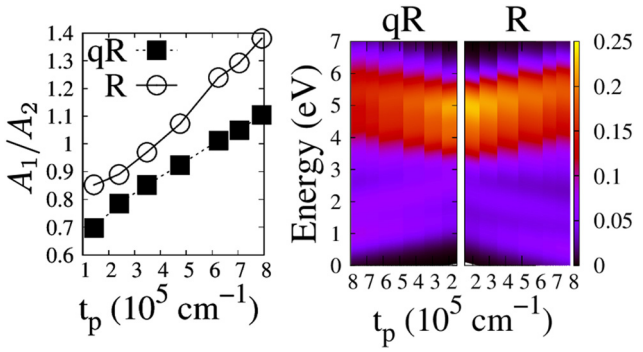

Fig. 4 The simulated A_1/A_2 ratio (left panel) and the absorption energy and intensity (right panel) at the quasi-resonance (qR) and resonance (R) regimes as a function of the transfer integral product $t_p = t_h \times t_e$. The full set of parameters is reported in the ESI,† Table S1.

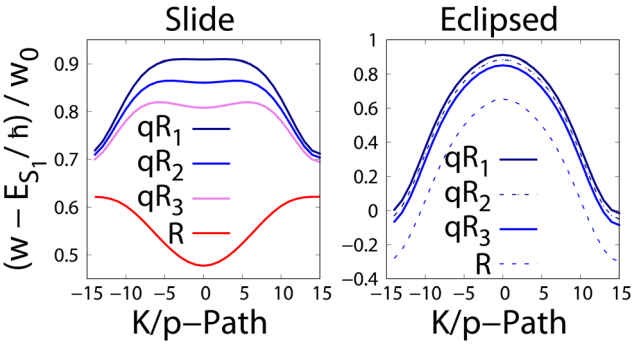

Fig. 5 Momentum(k)–exciton (E) dispersion profiles as a function of the energy difference E_{T-S_1}. Left (right) panel corresponds to the slide (eclipsed) configuration between consecutive monomers. The full set of parameters is reported in the ESI,† Table S2.

meaning that the J-aggregation signature may be modulated according to both the interaction strength between consecutive SBUs and energy difference E_{T-S_1}. The implication is the potential use of the absorption spectrum to screen different aggregates for photoconductive purposes. It is therefore useful to map the energy values spanned by the absorption spectra as a function of t_p, as illustrated in the right panel of Fig. 4. Here, one can recognize the regions of the highest and lowest intensities (dark regions) in both regimes. However, a closer look reveals that the spectrum in the R regime is slightly red shifted with respect to the one in the qR regime.

4.2. Vertical mobility

4.2.1. Effect of the quantum confinement on the carrier mobility. Vertical confinement and proximity effects,[21] manifested in the parameters L_z and S, may also be employed to manipulate vertical charge mobility in ultra-thin 2D MOFs and hence engineer desired photoconductive properties. It is thus insightful to first establish the relationship between the thickness of the film and the resistivity (ρ)[32,33] when a progressive vertical exfoliation reaches the quantum well (QW) limit (see the ESI,† Fig. S1). By definition, as long as the exfoliation does not alter carriers motion in any of the three dimensions, ρ displays bulk characteristics. At certain L_z value, the strong 2D confinement starts altering carriers flow. As a result, ρ starts increasing because of the decreasing relaxation time (*i.e.*, the average time between two consecutive scattering events). However, when the progressive exfoliation reaches the point where the De Broglie wavelength of the bound carrier (typically in the range $\lambda_\omega \sim$ 1–10 nm (ref. 34)) becomes comparable to the QW thickness, a dramatic drop in resistivity is observed and quantum phenomena begin to dominate physical properties of the material.[35]

Vertical quantum confinement increases absorption efficiency, which results from the strongly bound elect€(e)–hole(h) paired quasiparticles due to the weaker dielectric screening in a nanometer thickness.[36,37] Further, the enhanced exciton binding energy exerts a significant influence on both the energy transport and optical characteristics within the material. Insights into exciton dynamics may be obtained from the momentum (k)–energy (E) dispersion relation. For a given k, the J_{Coul}/T mixing can be studied by applying the dispersion relation[38]

$$E_{\pm}(k) = E_J(k) + \frac{E_T - E_J(k)}{2} \pm \sqrt{\left(\frac{E_T - E_J(k)}{2}\right)^2 + 2(t_e^2 + t_h^2 + 2t_h t_e \cos(k))} \quad (8)$$

where the exciton delocalization energy $E_J(k)$ is evaluated as a function of the coulombic interaction[39]

$$E_J(k) = E_{S_1} + 2J_{Coul}\cos(k) \quad (9)$$

where E_{S_1} corresponds to the energy of the $S_0 \rightarrow S_1$ electronic transition. In eqn (9), the wave vector k is in $1/S$ units and takes on the values $k = 0, \pm 2\pi/N, \pm 4\pi/N, \ldots, \pi$ and only the nodeless exciton with wave vector $k = 0$ is optically allowed. Hence, depending on the negative (positive) sign of J_{Coul}, the transition energy is lower (higher) than the monomeric transition energy, resulting in aggregation induced red (blue) shift in the optical absorption spectrum of J(H)-aggregates. Fig. 5 shows for L_z = 5.94 nm in the slide and eclipsed configurations how the k–E dispersion varies by progressively decreasing the energy difference E_{T-S_1}, from qR_1 to qR_3, until the R regime is reached (values are reported in Table S2, ESI†). While the eclipsed configuration is barely affected by the E_{T-S_1} progression, in the slide situation the spectra shift from blue to red. However, it is worth mentioning that these profiles may change in the presence of defects, which may trap carriers in localized states, thus effectively modulating the resistance of the material.

4.2.2. Tailoring the vertical mobility. Now, we turn our attention to evaluating the charge carrier mobility along the vertical dimension in ultra-thin $Ni_3(HITP)_2$ subjected to progressive exfoliation. Assuming that an external electric field along the π-stacking direction is applied to our model $Ni_3(HITP)_2$, as depicted in Fig. 6, charge carriers move with a wavelength λ_ω while experiencing the periodic potential variation due to the periodic arrangement of the atoms along the stacking direction. The net force on the carrier is due to

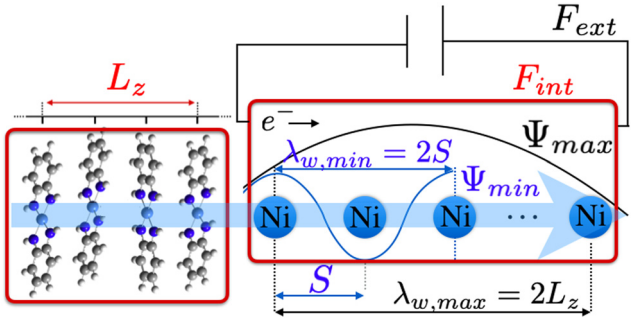

Fig. 6 Representation of a carrier moving along the π-stacking direction and experiencing the crystal field (F_{int}) which varies as a function of the inter-layer spacing S. The carrier wavelength ranges between $\lambda_{\omega,min} = 2S$ and $\lambda_{\omega,max} = 2L_z$.

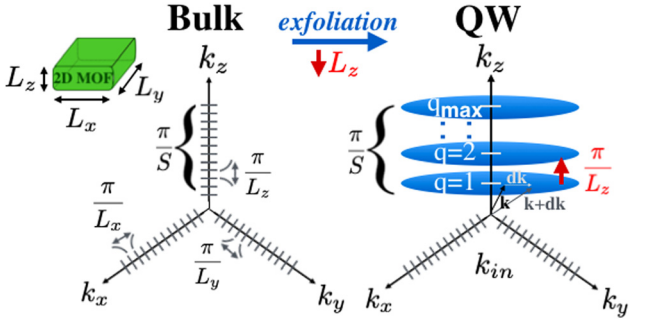

Fig. 7 Representation of the allowed states in the $Ni_3(HITP)_2$ thin layer in the k-space. By exfoliating L_z, the k_z step increases such that the number of allowed states along z becomes highly discretized. Yet, in the xy-plane the number of allowed states $k_{in} = k_x \times k_y$ remains very large. The blue planes correspond to the space of allowed states (*i.e.*, no states are permitted between them).

$F = F_{ext} + F_{int}$, where F_{int} corresponds to the crystal field. The response to in $Ni_3(HITP)_2$ is notably influenced by the metal d bands, as the latter plays a prime role in forming the direct/indirect band gap *via* the s–d and p–d couplings,[40,41] thus establishing photoconductive properties of the material. Provided the expression for the effective mass $m^* = \left(\frac{1}{\hbar^2}\frac{\partial^2 E}{\partial k^2}\right)^{-1}$, the crystal field is already taken into account in the Bloch's wavefunction and the crystal momentum $p = \hbar k$ responds only to F_{ext}, *i.e.* as if it was a free particle (more details can be found in the ESI,† Section S1). However, as displayed in Fig. 6, the physical confinement caused by the medium automatically restricts the oscillatory period of the wavefunction. This means that the round trip phase of the latter must be a multiple integer of 2π, according to the standing condition:

$$2kr = Q \cdot 2\pi \quad Q = 1, 2, 3\ldots \tag{10}$$

where the factor 2 on the LHS denotes the completion of a round trip phase kr. If we consider the three orthogonal components of the wavevector $\mathbf{k} \equiv (k_x, k_y, k_z)$, as a result of the spatial confinement $\lambda_\omega^q = 2L_z/q$, the k component along the stacking direction can assume a set of values as:

$$k_z^q = \frac{2\pi}{\lambda_\omega^q} = q\frac{\pi}{L_z}, \quad q = 1, 2, 3\ldots \tag{11}$$

Then, one can calculate the minimum and the maximum values of k_z using L_z or S in the denominator, respectively. For instance, if we assume a device with $L_z = 1$ mm, the smallest k_z value corresponds to $k_{z,min} = \frac{\pi}{1\,\text{mm}} = 10^3\,\pi\,\text{m}^{-1}$. On the other hand, considering the experimental[15] value of S = 3.3 Å in $Ni_3(HITP)_2$, $k_{z,max} = \frac{\pi}{S} = 3.0 \times 10^9\,\pi\,\text{m}^{-1}$, which means that the number of allowed states along k_z may vary as 10^6 orders of magnitude (in steps of $10^3\,\pi\,\text{m}^{-1}$) between the edges of the first Brillouin zone, see Fig. 7. Progressive exfoliation of L_z down to the QW limit, *i.e.* region (c) in Fig. S1 in the ESI,† leads to a dramatic discretization of the allowed states along k_z. For example, if L_z reaches ≈1 nm, the number of allowed states along z reduces to only 3 with $k_z^1 = \frac{\pi}{10\,\text{Å}}$, $k_z^2 = 2 \times \frac{\pi}{10\,\text{Å}} = \frac{\pi}{5\,\text{Å}}$, and $k_z^3 = 3 \times \frac{\pi}{10\,\text{Å}} \approx \frac{\pi}{3.3\,\text{Å}}$. As a result, as presented in Table 1, the densities of states become directly dependent on L_z, see the ESI,† Section S1 for the corresponding derivations.

Table 1 Expressions for the bulk and QW densities in k and E_c (conduction band) spaces (for derivations see the ESI, Section S1)

	Bulk	QW
$D(k)$	$\frac{k^2}{\pi^2}$	$\frac{k}{\pi L_z}$
$D(E_c)$	$\frac{1}{2\pi^2}(E - E_c)^{\frac{1}{2}}\left(\frac{2m_c^*}{\hbar^2}\right)^{\frac{3}{2}}$	$\frac{m_c^*}{\hbar^2 \pi L_z}$

For photoconductive engineering purposes, Fig. S3 (ESI†) shows how the discretization along k_z can be used to tailor the effective band gap[34,42] E_g^{eff} as a function of L_z. Assuming the same value for m^* in both conduction and valence bands, the relationship can be formulated as:

$$E_g^{eff} = E_g^{bulk} + \frac{\hbar^2 k_z^2}{m^*} = E_g^{bulk} + \left(\frac{\hbar^2}{m^*}\right)\left(\frac{\pi^2}{L_z^2}\right). \tag{12}$$

Eqn (12) can be used as a guideline for evaluating the threshold L_z values below which quantum mechanical effects would dictate the photoconductive properties of the material. Nevertheless, under *operando* conditions, it is not possible to attain the desired photoconductive attributes solely by adjusting L_z. In such scenarios, the carrier mobility is also affected by imperfections. These imperfections can be categorized into two main types (or combinations of both): point imperfections resulting from atoms being out of place within the 2D structure due to temperature effects (commonly referred to as defects), and larger dislocations caused by the relative lateral movement between layers.

4.2.3. Gauging the hopping rate. If the $Ni_3(HITP)_2$ stacking was well-ordered and free from any imperfections, the carrier wavefunctions would be delocalized over many units and a through-band transport could be attained. Yet, even in well-ordered chains of conjugated units, macroscopic transport is

governed by hopping mechanism due to presence of imperfections and defects.[43] Ours and others works has firmly established that layer-layer displacements in 2D MOFs are a major source of imperfection.[13,14,44] Specifically, very recently, we have shown[20] the effect of the relative sliding between layers and their corresponding geometrical changes on the absorption spectra of 2D MOFs as they can be gauged by evaluating transfer integrals (t) and reorganization energy (λ), respectively. Briefly, the geometrical changes in the units of our $Ni_3(HITP)_2$ model, when going from neutral to excited/charged states, can be gauged by calculating an effective Huang–Rhys factor λ_{eff} (in the harmonic approximation):[45]

$$\lambda_{\text{eff}} = \sum_i \lambda_i \lambda_i = \frac{m_i \omega_i}{2\hbar} R_i^2 \tag{13}$$

where ω_i represents the frequency of the normal mode i while R_i is the projection of the displacements between equilibrium geometries of the neutral and radical-cation or radical-anion states (hereafter, for the sake of brevity, we refer to λ_{eff} simply as the reorganization energy λ). Eventually, whether a band-like or hopping transport mechanism is operative, charge-transport characteristics depend on both λ and t parameters.[46,47] Since Marcus rate theory suggests that the inter-unit charge transfer and the hopping rate can be determined by these parameters,[48–51] it serves as a beneficial tool for investigating carrier mobility in 2D MOF nanosheets. Here, we evaluate vertical hopping rates μ_T along the stacking direction according to the expression:

$$\mu_T = \frac{4\pi^2}{h} \frac{1}{\sqrt{4\pi k_B T}} t_{h,e}{}^2 \exp\left(-\frac{(\Delta G + \lambda)^2}{4\lambda k_B T}\right) \tag{14}$$

where $t_{h,e}$ may represent the carrier tunneling rate and the exponential factor rules the activation energy or the energy barrier for the charge transfer between two consecutive units. With the aim of evaluating the effect of inter-layer proximity on the carrier hopping along the π-stacking direction in the nanosheet, we maintain the same value of L_z = 5.94 nm as in Fig. 2 except that now we vary the total number of units N hence changing the inter-layer distance S. Fig. 8 illustrates the increasing trend for electron mobility with decreasing S at three different temperatures of T_1 = 290 K, T_2 = 296 K, and T_3 = 298 K. This is the direct result of modulating vdW interactions between layers by manipulating the inter-layer distance. The increasing trend of μ_T with respect to T shows that the electron mobility is temperature-driven with the lowest hopping rate obtained at T_1 = 290 K and S = 3.96 Å and the highest found at T_3 = 298 K and S = 3.3 Å. Fig. 8 also provides insights on the effects of crystal packing on charge mobility. While the black profiles depict μ_T values obtained for an eclipsed arrangement of the units in the stacking direction, blue profiles correspond to a slipped-parallel packing with the slipping distance of 1.8 Å, as previously reported.[11] As can be seen, the slipped-parallel packing leads to smaller μ_T values compared to the eclipsed packing at the same inter-layer distance. The difference between blue and black profiles also increases with temperature. Overall, eclipsed packing seems to enhance vdW interactions and the vertical charge transfer rate *via* the hopping mechanism. Fig. 9 shows the estimated difference between

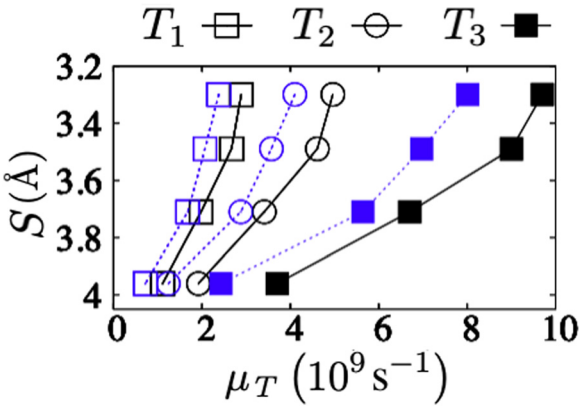

Fig. 8 Electron transfer rates μ_T in $Ni_3(HITP)_2$ as a function of the inter-layer spacing S at different temperatures of T_1 = 290 K, T_2 = 296 K, and T_3 = 298 K. Black profiles correspond to the eclipsed packing whereas the blue profiles refer to the slipped-parallel packing. All parameters and their corresponding units are reported in the ESI,† Tables S2–S4.

electron and hole mobility in the $Ni_3(HITP)_2$ nanosheet. The hole mobility generally surpasses or is at least comparable to the electron mobility. This observation may appear unexpected under the influence of, which restricts hole movement more than electron motion because of the stronger atomic force exerted by the nucleus on holes compared to electrons located in outer shells. Nonetheless, in the case of $Ni_3(HITP)_2$, our analysis reveals that the lowest unoccupied molecular orbital (LUMO) wavefunction exhibits an additional node compared to the highest occupied molecular orbital (HOMO) wavefunction.[20] Since the splitting in each frontier orbital depends on the number of nodes,[52] in $Ni_3(HITP)_2$ the LUMO splitting is expected to be smaller (leading to higher m_c^*) than the HOMO splitting and qualitatively this difference translates into larger HOMO bandwidths and higher hole mobility. In turn, this difference is crucial in both optical upward and downward transitions and recombination processes within the nanosheet.[53]

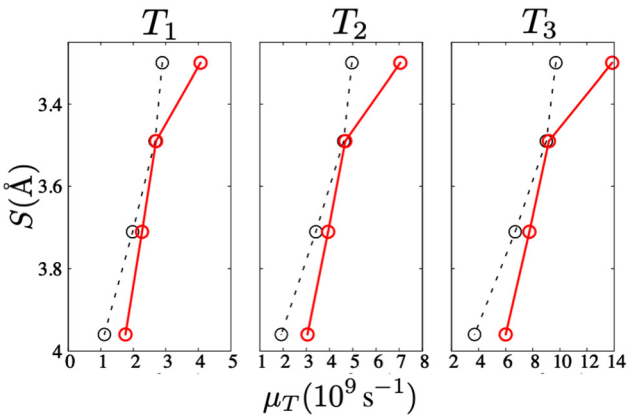

Fig. 9 Comparison between electron (black) and hole (red) transfer rates in the $Ni_3(HITP)_2$ nanosheet as a function of the inter-layer spacing S at different temperatures of T_1 = 290 K, T_2 = 296 K, and T_3 = 298 K. All parameters and their corresponding units are reported in the ESI,† Tables S2–S4.

5. Conclusions

In this study, we have demonstrated how theoretical models and concepts can offer valuable insights into leveraging spatial confinement and inter-layer proximity to modulate optical properties and vertical mobility in ultra-thin 2D MOFs. These insights are instrumental in guiding the design and synthesis of precisely defined 2D MOF nanosheets with meticulous control over their structures and compositions. While achieving precise control over nanostructures remains a formidable task that is still in its nascent stages, promising avenues may emerge through the integration of synthetic chemistry with electronic structure computations and transport measurements to unravel the relationships between structure and photoconductivity in 2D MOF nanosheets.

Data availability

The data supporting this article have been included as part of the ESI.† Additional data are available from the corresponding authors upon reasonable request.

Conflicts of interest

There are no conflicts to declare.

Acknowledgements

This research has been partially enabled by the use of computing resources and technical support provided by the HPC center at New Jersey Institute of Technology (NJIT), US and partially enabled by the use of the HPC resources of TGCC under the allocation 2023-A0140810433 made by GENCI. David Dell'Angelo thanks Professor Farnaz Shakib from NJIT for support and discussions. This study was also developed in the framework of the research activities carried out within the Project ''Network 4 Energy Sustainable Transition—NEST'', Spoke 1, Project code PE0000021, funded under the National Recovery and Resilience Plan (NRRP).

References

1 M. Ko, L. Mendecki and K. A. Mirica, *Chem. Commun.*, 2018, **54**, 7873–7891.
2 L. S. Xie, G. Skorupskii and M. Dincă, *Chem. Rev.*, 2020, **120**, 8536–8580.
3 X. Wang, X. Zhang, W. Zhou, L. Liu, J. Ye and D. Wang, *Nano Energy*, 2019, **62**, 250–258.
4 Z. Wang, M. He, H. Jiang, H. He, J. Qi and J. Ma, *Chem. Eng. J.*, 2022, **435**, 133870.
5 Z. W. Jiang, T. T. Zhao, S. J. Zhen, C. M. Li, Y. F. Li and C. Z. Huang, *J. Mater. Chem. A*, 2021, **9**, 9301–9306.
6 W.-M. Liao, J.-H. Zhang, S.-Y. Yin, H. Lin, X. Zhang, J. Wang, H.-P. Wang, K. Wu, Z. Wang, Y.-N. Fan, M. Pan and C.-Y. Su, *Nat. Commun.*, 2018, **9**, 2401.
7 W. Pang, B. Shao, X.-Q. Tan, C. Tang, Z. Zhang and J. Huang, *Nanoscale*, 2020, **12**, 3623–3629.
8 G. Chakraborty, I.-H. Park, R. Medishetty and J. Vittal, *Chem. Rev.*, 2021, **121**, 3751–3891.
9 Y. Liang, R. Shang, J. Lu, L. Liu, J. Hu and W. Cui, *ACS Appl. Mater. Interfaces*, 2018, **10**, 8758–8769.
10 M. Zhao, Y. Huang, Y. Peng, Z. Huang, Q. Ma and H. Zhang, *Chem. Soc. Rev.*, 2018, **47**, 6267–6295.
11 D. Sheberla, L. Sun, M. A. Blood-Forsythe, S. Er, C. R. Wade, C. K. Brozek, A. Aspuru-Guzik and M. Dincă, *J. Am. Chem. Soc.*, 2014, **136**, 8859–8862.
12 T. Chen, J.-H. Dou, L. Yang, C. Sun, N. J. Libretto, G. Skorupskii, J. T. Miller and M. Dincă, *J. Am. Chem. Soc.*, 2020, **142**, 12367–12373.
13 M. E. Foster, K. Sohlberg, M. D. Allendorf and A. A. Talin, *J. Phys. Chem. Lett.*, 2018, **9**, 481–486.
14 Z. Zhang, D. Dell'Angelo, M. R. Momeni, Y. Shi and F. A. Shakib, *ACS Appl. Mater. Interfaces*, 2021, **13**, 25270–25279.
15 R. W. Day, D. K. Bediako, M. Rezaee, L. R. Parent, G. Skorupskii, M. Q. Arguilla, C. H. Hendon, I. Stassen, N. C. Gianneschi, P. Kim and M. Dincă, *ACS Cent. Sci.*, 2019, **5**, 1959–1964.
16 K. N. Le and C. H. Hendon, *Phys. Chem. Chem. Phys.*, 2019, **21**, 25773–25778.
17 G. Sfuncia, G. Nicotra, F. Giannazzo, B. Pécz, G. K. Gueorguiev and A. Kakanakova-Georgieva, *CrystEngComm*, 2023, **25**, 5810–5817.
18 Z. Wang, G. Wang, H. Qi, M. Wang, M. Wang, S. Park, H. Wang, M. Yu, U. Kaiser, A. Fery, S. Zhou, R. Dong and X. Feng, *Chem. Sci.*, 2020, **11**, 7665–7671.
19 Z. Li, X. Zhang, H. Cheng, J. Liu, M. Shao, M. Wei, D. G. Evans, H. Zhang and X. Duan, *Adv. Energy Mater.*, 2020, **10**, 1900486.
20 D. Dell'Angelo, M. R. Momeni, S. Pearson and F. A. Shakib, *J. Chem. Phys.*, 2022, **156**, 044109.
21 A. Kuc, M. A. Springer, K. Batra, R. Juarez-Mosqueda, C. Wöll and T. Heine, *Adv. Funct. Mater.*, 2020, **30**, 1908004.
22 M. J. Kalmutzki, N. Hanikel and O. M. Yaghi, *Sci. Adv.*, 2018, **4**, eaat9180.
23 H. S. Lee, S.-W. Min, Y.-G. Chang, M. K. Park, T. Nam, H. Kim, J. H. Kim, S. Ryu and S. Im, *Nano Lett.*, 2012, **12**, 3695–3700.
24 T. Holstein, *Ann. Phys.*, 1959, **8**, 325–342.
25 F. C. Spano, *Acc. Chem. Res.*, 2010, **43**, 429–439.
26 N. J. Hestand and F. C. Spano, *Acc. Chem. Res.*, 2017, **50**, 341–350.
27 R. D. Harcourt, G. D. Scholes and K. P. Ghiggino, *J. Chem. Phys.*, 1994, **101**, 10521–10525.
28 R. D. Harcourt, K. P. Ghiggino, G. D. Scholes and S. Speiser, *J. Chem. Phys.*, 1996, **105**, 1897–1901.
29 E. E. Jelley, *Nature*, 1936, **138**, 1009.
30 C. Allolio, T. Stangl, T. Eder, D. Schmitz, J. Vogelsang, S. Höger, D. Horinek and J. M. Lupton, *J. Phys. Chem. B*, 2018, **122**, 6431–6441.
31 F. C. Spano, *J. Chem. Phys.*, 2005, **122**, 234701.
32 K. Takayanagi, Y. Kondo and H. Ohnishi, *JSAP Int.*, 2001, **3**, 3.

33 S. Datta, *Electronic transport in mesoscopic systems*, Cambridge University Press, Cambridge, 1995.
34 A. C. Berends and C. de Mello Donega, *J. Phys. Chem. Lett.*, 2017, **8**, 4077–4090.
35 E. Li, B. Weiss and K.-S. Chan, *IEEE J. Quantum Electron.*, 1996, **32**, 1399–1416.
36 K. F. Mak, C. Lee, J. Hone, J. Shan and T. F. Heinz, *Phys. Rev. Lett.*, 2010, **105**, 136805.
37 K. Mak, K. He, C. Lee, G.-H. Lee, J. Hone, T. Heinz and J. Shan, *Nat. Mater.*, 2012, **12**, 207.
38 N. J. Hestand and F. C. Spano, *J. Chem. Phys.*, 2015, **143**, 244707.
39 J. Frenkel, *Phys. Rev.*, 1931, **37**, 17–44.
40 L.-P. Tang, L.-M. Tang, H. Geng, Y.-P. Yi, Z. Wei, K.-Q. Chen and H.-X. Deng, *Appl. Phys. Lett.*, 2018, **112**, 012101.
41 L.-D. Yuan, H.-X. Deng, S.-S. Li, S.-H. Wei and J.-W. Luo, *Phys. Rev. B*, 2018, **98**, 245203.
42 K. Tanaka and T. Kondo, *Sci. Technol. Adv. Mater.*, 2003, **4**, 599–604.
43 R. S. Kohlman and A. J. Epstein, *Handb. Conduct. Polym.*, 1986, **1**, 85.
44 M. E. Foster, K. Sohlberg, C. D. Spataru and M. D. Allendorf, *J. Phys. Chem. C*, 2016, **120**, 15001–15008.
45 L. Gisslén and R. Scholz, *Phys. Rev. B: Condens. Matter Mater. Phys.*, 2009, **80**, 115309.
46 W.-Q. Deng and W. A. Goddard, *J. Phys. Chem. B*, 2004, **108**, 8614–8621.
47 G. R. Hutchison, M. A. Ratner and T. J. Marks, *J. Am. Chem. Soc.*, 2005, **127**, 2339–2350.
48 R. A. Marcus, *Rev. Mod. Phys.*, 1993, **65**, 599.
49 R. A. Marcus, *Adv. Chem. Phys.*, 1999, **106**, 1.
50 J. L. Brédas, J. P. Calbert, D. A. da Silva Filho and J. Cornil, *Proc. Natl. Acad. Sci. U. S. A.*, 2002, **99**, 5804–5809.
51 P. F. Barbara, T. J. Meyer and M. A. Ratner, *J. Phys. Chem.*, 1996, **100**, 13148.
52 Y. Kashimoto, K. Yonezawa, M. Meissner, M. Gruenewald, T. Ueba, S. Kera, R. Forker, T. Fritz and H. Yoshida, *J. Phys. Chem. C*, 2018, **122**, 12090–12097.
53 G. Xing, B. Wu, X. Wu, M. Li, B. Du, Q. Wei, J. Guo, E. Yeow, T. C. Sum and W. Huang, *Nat. Commun.*, 2017, **8**, 14558.